Broadband terahertz absorber with various tunable functions based on double-layer graphene

HANMO DU[1], XIN ZHANG[1], JIA LIU[1], HONGYAN MENG[1,2], SHUANG YANG[1], YACHEN GAO[1,*]
[1]*Electronic Engineering College, Heilongjiang University, Harbin, 150080, China*
[2]*College of Communication and Electronic Engineering, Qiqihar University, Qiqihar 161000, China*

A terahertz (THz) metasurface absorber using double-layer graphene achieves broadband absorption with over 90% absorptance in 5.02–9.13 THz, offering a 4.11 THz bandwidth. Finite-difference time-domain (FDTD) simulations reveal that the combined effects of disk- and square-shaped graphene enable modulation of absorptance at low and high frequencies by adjusting the Fermi energy (E_F), achieving absorption intensity from 11% to 100%. The absorber maintains broadband performance under varying SiO_2 thickness, azimuthal angles, and incident angles, ensuring robustness and tunability.

(Received December 13, 2024; accepted June 3, 2025)

Keywords: Tunable, Terahertz, Graphene, Broadband absorption

1. Introduction

Terahertz (THz) waves refer to electromagnetic waves with frequencies ranging from 0.1 to 10 THz. Due to their advantages of high transmittance, low energy, noninvasive, and nonionizing properties [1], THz waves have received tremendous and growing attention in the fields of non-destructive testing [2], biomedicine [3, 4], security [5], telecommunications [6], sensing [7], and so on. However, since natural materials cannot effectively respond to THz waves, the development of THz technology was stalled until the emergence of metamaterials. As an artificial material composed of subwavelength periodic arrays [8], metamaterials have become a research hotspot in recent years due to their extraordinary physical properties lacking in natural materials [9, 10].

The absorption of electromagnetic waves is an important branch of electromagnetic wave regulation [11, 12], which is being promoted in various fields such as photo-detectors [13], saturable absorbers [14], and photovoltaics [15]. Therefore, various THz absorbers with diverse structures and types have been designed and proposed by researchers. In 2008, Landy et al. designed the first perfect absorber, which consisted of an electric resonator and cut wire [16]. In the same year, Tao et al. proposed a metamaterial absorber working in the THz band to achieve narrow-band absorption [17]. Since then, dielectric metasurface absorbers [18], metal metasurface absorbers [19], etc., have emerged one after another. However, once the structure of the traditional absorber is determined, the adjustment of the absorption characteristics becomes a difficult problem. Therefore, the development of tunable THz absorbers is imperative to adapt to a wider range of practical applications.

Graphene is a novel two-dimensional material with unique electro-optical properties [20]. Changing its bias voltage or chemical doping can dynamically adjust its carrier mobility, this leads to a change in the Fermi energy level (E_F) of graphene, and then achieve the purpose of controlling the absorption frequency of the absorber [21-23]. Therefore, graphene proves to be a fitting material for designing tunable THz absorbers. In 2018, Zhou et al. designed a controllable broadband absorber utilizing a sinusoidal 1rapheme layer, achieving an absorption window of 0.5 THz and an intensity modulation from 40% to 90% [24]. In 2020, Liu et al. designed an ultra-broadband absorber composed of multilayer graphene, achieving an absorption window of 1.12-3.78THz [25]. In 2021, Xu et al. designed a broadband tunable absorber based on windmill graphene and complete graphene, achieving a broadband absorption of 1.96 THz and an intensity modulation from 52% to 100% [26]. In 2022, Wang et al. designed an ultra-broadband absorber, by making the graphene layer periodically modulated along the x-axis, a record ultra-broadband absorption of 3.71 THz is achieved [27]. In 2023, Ren et al. proposed a broadband absorber composed of gold disks and patterned graphene, achieving an absorption window of 4.6-7.7 THz and center frequency shift of 1.15 THz [28]. In the same year, Ding et al. proposed an ultra-broadband absorber composed of multi-square rings graphene, achieving an absorption window of 4.12-7.16 THz and an intensity modulation from 15% to 100% [29]. In 2024, Sur et al. designed a polarization-insensitive graphene metasurface absorber [30]. The top layer of the absorber consists of nine circularly patterned graphene units, while

the middle layer is a square graphene interlayer. This structure achieves over 90% efficient absorption within the frequency range of 1.96 to 5.72 THz. Additionally, by tuning the parameters of the graphene layers, diverse absorption modes can be realized. However, the aforementioned graphene-based absorbers still necessitate a broader working bandwidth in the THz range to meet the demands of practical applications. There is still considerable room for improvement in both working bandwidth and modulation. Therefore, comprehensive research on absorbers with multifunctional tunability and augmented working bandwidth is imperative.

In this work, a THz metasurface absorber utilizing double-layer graphene is proposed to achieve broadband absorption. The absorption characteristics of the absorber were theoretically studied. Compared with other graphene-based broadband absorbers, the designed absorber shows an expanded absorption bandwidth, achieving an absorbance of more than 90% in the range of 5.02-9.13 THz. By changing the bias voltage of graphene, two layers of graphene are utilized for independently or concurrently modulating the absorptance at low and high frequencies. And the absorption performance of the absorber shows no sensitivity to either azimuthal angle or incident angle. Due to the advantageous characteristics of the designed THz absorber, it shows potential applications in stealth technology, electromagnetic interference shielding, medical imaging, and solar cells.

2. Structure and method

Fig. 1 shows the structure unit of the designed broadband absorber. As shown in Fig. 1(a), the structure unit is comprised of disk-shaped graphene, SiO_2, square-shaped graphene, SiO_2, and gold layers from top to bottom. In order to control the bias voltage of graphene more conveniently, as shown in Fig. 1(b-c), the disk-shaped graphene is designed to be tangent, and the square-shaped graphene is connected by slim graphene nanoribbons. P_x and P_y represent the period of the unit cell, r represents the radius of the disk-shaped graphene, W represents the length of the square-shaped graphene, t_1 and t_2 represent the thickness of the upper and lower SiO_2 layers respectively. The parameters are set as follows: $P_x = P_y = 3\ \mu m$, $r = 1.5\ \mu m$, $W = 1.8\ \mu m$, $t_1 = 1.6\ \mu m$, $t_2 = 4.9\ \mu m$, the thickness of the gold layer is set to be $0.5\ \mu m$ and the conductivity is set to be $4.561 \times 10^7\ S/m$ determined by the static model [31].

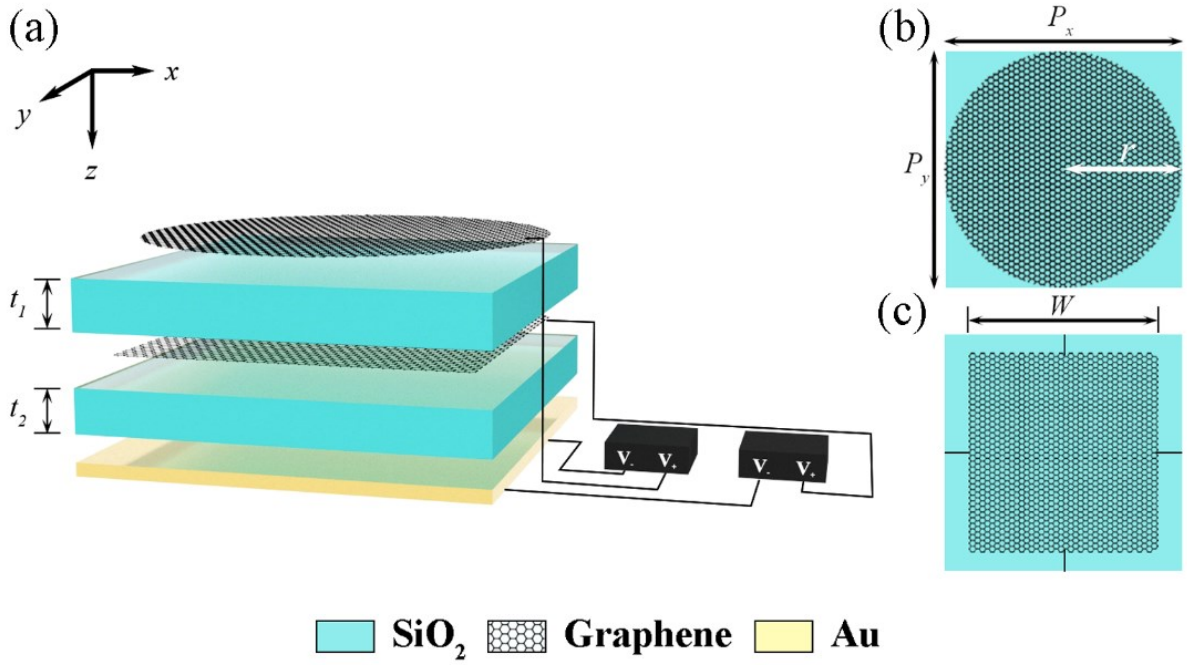

Fig. 1. (a) Three-dimensional structure unit diagram of the proposed absorber. (b) The top views of the disk-shaped graphene layer and c) square-shaped graphene layer (colour online)

In this work, the absorptance of the absorber is theoretically studied by using the finite-difference time-domain (FDTD) method. The x-axis and y-axis directions are configured with periodic boundary conditions, while the z-axis direction is configured with a perfectly matched layer. The absorptance of the structure can be obtained from [32]:

$$A(\omega) = 1 - R(\omega) - T(\omega) \tag{1}$$

where $R(\omega)$ and $T(\omega)$ represents the reflectance and

transmittance respectively. Here, $R(\omega) = |S_{11}(\omega)|^2$ and $T(\omega) = |S_{21}(\omega)|^2$, with $S_{11}(\omega)$ and $S_{21}(\omega)$ being the reflection parameters and transmission parameters of the absorber which can be extracted based on the FDTD method. Since the gold layer's thickness exceeds the skin depth of the THz wave, it can be assumed that all waves in the frequency range are reflected [33]. As a result, the transmittance $T(\omega)$ is approximately equal to 0. Therefore, the equation is capable to be rewritten as:

$$A(\omega) = 1 - R(\omega) = 1 - |S_{11}(\omega)|^2 \tag{2}$$

The surface conductivity of graphene is conposed of intraband and interband conductivity, which can be determined by the KUBO formula as follows [34, 35]:

$$\sigma(\omega, \mu_c, \Gamma, T) = \sigma_{intra} + \sigma_{inter} \tag{3}$$

$$\sigma_{intra} = \frac{je^2}{\pi\hbar^2(\omega - j2\Gamma)} \int_0^\infty \xi \left(\frac{\partial f_d(\xi, \mu_c, T)}{\partial \xi} - \frac{\partial f_d(-\xi, \mu_c, T)}{\partial \xi} \right) \mathrm{d}\xi \tag{4}$$

$$\sigma_{inter} = -\frac{je^2(\omega - 2\Gamma)}{\pi\hbar^2} \int_0^\infty \frac{f_d(-\xi, \mu_c, T) - f_d(\xi, \mu_c, T)}{(\omega - j2\Gamma)^2 - 4(\xi/\hbar)^2} \mathrm{d}\xi \tag{5}$$

$$f_d(\xi, \mu_c, T) = \left(e^{(\xi - \mu_c)/K_B T} + 1 \right)^{-1} \tag{6}$$

where σ is the conductivity, ω is the angular frequency of the incident radiation, μ_c is the chemical potential, $\Gamma = (2\tau)^{-1}$ is the scattering rate, T is the temperature with a value of 300 K in the simulation, e is the electron charge, $\hbar$ is the reduced Plank constant, ξ is the electron energy, and K_B is the Boltzmann constant.

Since the designed absorber works in the THz band, the corresponding photon energy $\hbar\omega \ll \mu_c$ [36]. Based on the Pauli exclusion principle, σ_{inter} can be disregarded. According to the Drude model, the graphene conductivity can be simplified into as follows [37]:

$$\sigma(\omega, \mu_c, \Gamma, T) = \frac{e^2 K_B T \tau}{\pi\hbar^2(1 + j\omega\tau)} \left\{ \frac{\mu_c}{K_B T} + 2\ln\left[exp\left(-\frac{\mu_c}{K_B T} \right) + 1 \right] \right\} \tag{7}$$

where τ is the electron-phonon relaxation time which is set to be 0.1 ps in the simulation. The Fermi energy level of graphene E_F can be approximated as [38]:

$$E_F = \mu_c \approx \hbar v_f \sqrt{\frac{\pi\varepsilon_r\varepsilon_0 V_g}{e t_s}} \tag{8}$$

where ε_r is the permittivity of SiO_2 which is set to be 3.9 in the simulation [39], ε_0 is the permittivity of vacuum, V_g is the bias voltage, and v_f is the Fermi velocity which is 1.1×10^6 m/s in graphene [40]. According to the equation, E_F can be tuned by changing the bias voltage from 0 eV to 1 eV.

3. Results and discussion

Fig. 2 shows the absorption spectrum of the designed absorber. The black line represents the absorptance of disk-shaped graphene layer (GL 1) and square graphene layer (GL 2) working simultaneously. At this time, the Fermi energy level of GL 1 (E_{F1}) and GL 2 (E_{F2}) are both set to 1eV. Broadband absorption with an absorbance of more than 90% in the range of 5.02-9.13 THz is achieved. Three peaks P_1, P_2, and P_3, appear at 5.41, 7.07, and 8.64 THz, respectively.

In order to preliminary analysis the origin of these three peaks, the absorptance of each GL working alone is also calculated, which is represented by the blue and red lines in the Fig. 2. It can be observed that P_1 is mainly contributed by GL 2, P_3 is mainly contributed by GL 1, and P_2 appears when GL 1 and GL 2 work together.

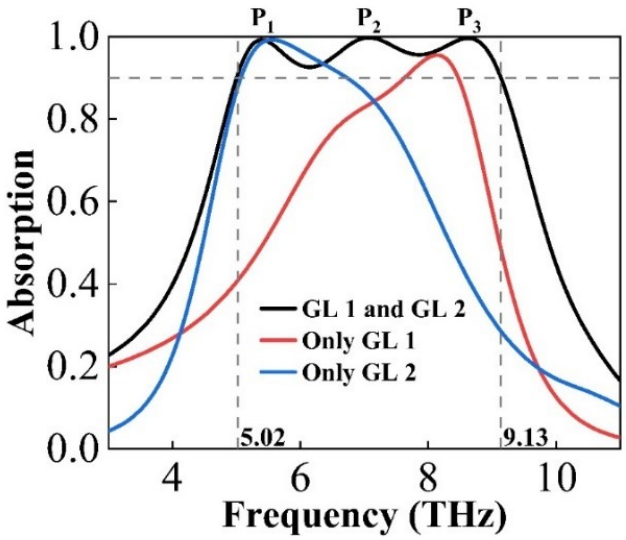

Fig. 2. The absorption spectrum when $E_{F1} = E_{F2} = 1$ eV (black line), only GL 1 (red line) and only GL 2 (blue line) (colour online)

To clarify the physical mechanism of the designed absorber, the electric field distribution of GL 1 and GL 2 at frequencies P_1 (5.41 THz), P_2 (7.07 THz) and P_3 (8.64 THz) is provided in Fig. 3. Fig. 3(a-c) demonstrates that the enhanced electric field of GL 1 is predominantly localized at its left and right ends. This phenomenon arises from the electric-dipole excitation occurring at the left and right ends of GL 1. Meanwhile, it can be seen from Fig. 3(d-f), the electric field of GL 2 is primarily concentrated at the edge of the graphene, which is a typical feature of localized surface plasmon resonance. As the frequency increases, the electric field of GL 1 continues to intensify while the electric field of GL 2 diminishes. This indicates that the absorption peak at P_1 is primarily attributed to GL 2, and the absorption peak at P_3 is mainly caused by GL 1. Therefore, the physical mechanism of broadband absorption is a combination of electric dipole resonance and localized surface plasmon resonance.

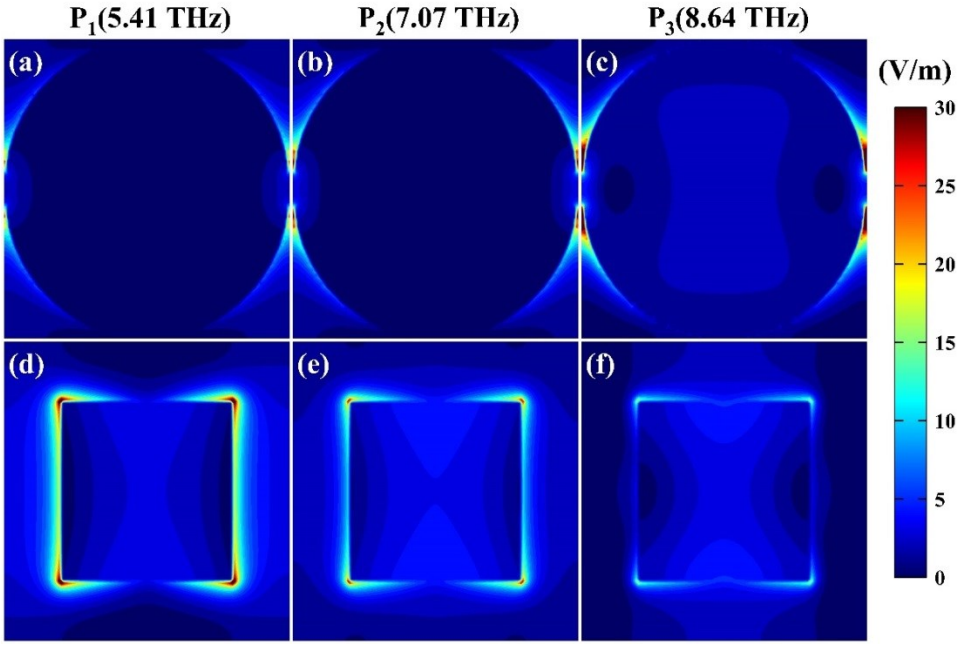

Fig. 3. Electric field distribution of (a-c) GL 1 and (d-f) GL 2 at 5.41, 7.07, and 8.64 THz in the x-y plane (colour online)

Next, we further analyzed the absorption mechanism of the designed absorber based on the impedance matching theory, which is expressed by the formula as [41]:

$$A(\omega) = 1 - \left|\frac{Z-Z_0}{Z+Z_0}\right|^2 = 1 - \left|\frac{Z_r-1}{Z_r+1}\right|^2 \tag{9}$$

$$Z_r = \pm\sqrt{\frac{\left(1+S_{11}(\omega)\right)^2 - S_{21}(\omega)^2}{\left(1-S_{11}(\omega)\right)^2 - S_{21}(\omega)^2}} \tag{10}$$

where Z is the impedance of the absorber, Z_0 is the free space impedance, and the relative impedance Z_r satisfies the relationship:

$$Z_r = \frac{Z}{Z_0} \tag{11}$$

As $Z = Z_0$, that is, $Z_r = 1$, the impedance achieves perfect matching with the free space impedance, and the absorptance reaches 100%. To achieve perfect absorption, it is necessary for the real part of the relative impedance to be equal to 1, and for the imaginary part to be equal to 0. Fig. 4 is the real part and imaginary part of the relative impedance of the proposed absorber. As shown in Fig. 4, the real part of the relative impedance, indicated by the solid black line, and the imaginary part, indicated by the dashed red line, closely approach 1 and 0 respectively within the range of 5.02-9.13 THz. This phenomenon indicates that the relative impedance of the designed absorber forms a good match with the free space impedance and is consistent with the simulation results, confirming the accuracy of the efficient broadband absorption of the designed absorber.

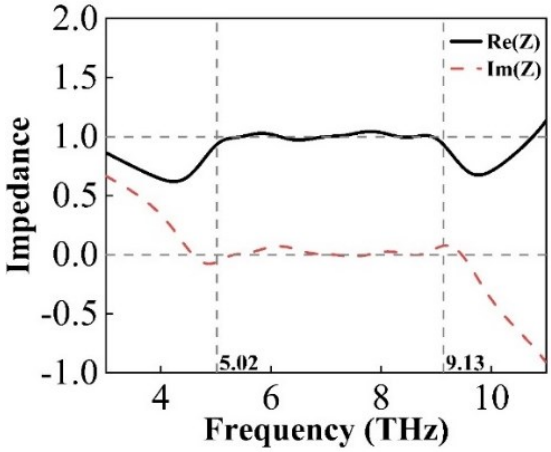

Fig. 4. Real part (solid black line) and imaginary part (dashed red line) of the relative impedance of the proposed absorber ($E_{F1} = E_{F2} = 1$ eV) (colour online)

Then, we investigated the tunability of the designed absorber. Fig. 5 shows the variations in relative impedance and absorbance when E_F of one graphene layer is set to be 0 eV while the other is changed. As depicted in Fig. 5(a-b), when E_{F1} is set to be 0 eV, and E_{F2} increases from 0 eV to 1 eV, the curves of the relative impedance of the absorber gradually approach perfect absorption in the low-frequency region, that is, the real part approximates 1 and the imaginary part approximates 0. This results in the absorbance of the absorber only retaining the low-frequency region. Consequently, the absorbance spectrum of the absorber is confined to the low-frequency range of 5.05-6.71 THz, as shown in Fig. 5(c). This behavior is attributed to the low E_{F1}, which attenuates the surface plasmon resonance of graphene, resulting in a reduction in high-frequency absorbance. Correspondingly, as shown in Fig. 5(d-e), when E_{F2} is set to be 0 eV, and E_{F1} increases from 0 eV to 1 eV, both the curves of the real and imaginary parts converge to 1 and 0 in the high-frequency region respectively. This eventually leads to the establishment of an absorption window ranging from 7.58-8.51 THz, as shown in Fig. 5(f).

The blue-shifting of the absorption peak during modulation with an increase in μ_{c1} and μ_{c2} can be attributed to an elevation in the resonant frequency of the absorber structure, which can be expressed as [26]:

$$\omega = 1.0/(LC)^{1/2} \tag{12}$$

where L is the total inductance of the absorber, and C is the total capacitance. The total inductance L can be defined as:

$$L = L_k + L_g \tag{13}$$

where L_k is the kinetic inductance, L_g is the constant inductance when the structure is fixed. The kinetic inductance L_k can be approximated as [42]:

$$L_k = \alpha(m_e/(N_d e^2)) \tag{14}$$

where α is a parameter associated with the structure, m_e is the electron mass, and N_d is the carrier concentration which is directly proportional to E_F. As E_F is increased, the carrier concentration N_d also rises. This leads to a decrease in the kinetic inductance L_k, consequently, a reduction of the total inductance L. Ultimately, this results in an increase in the resonant frequency ω, causing the absorption peak to blue-shift.

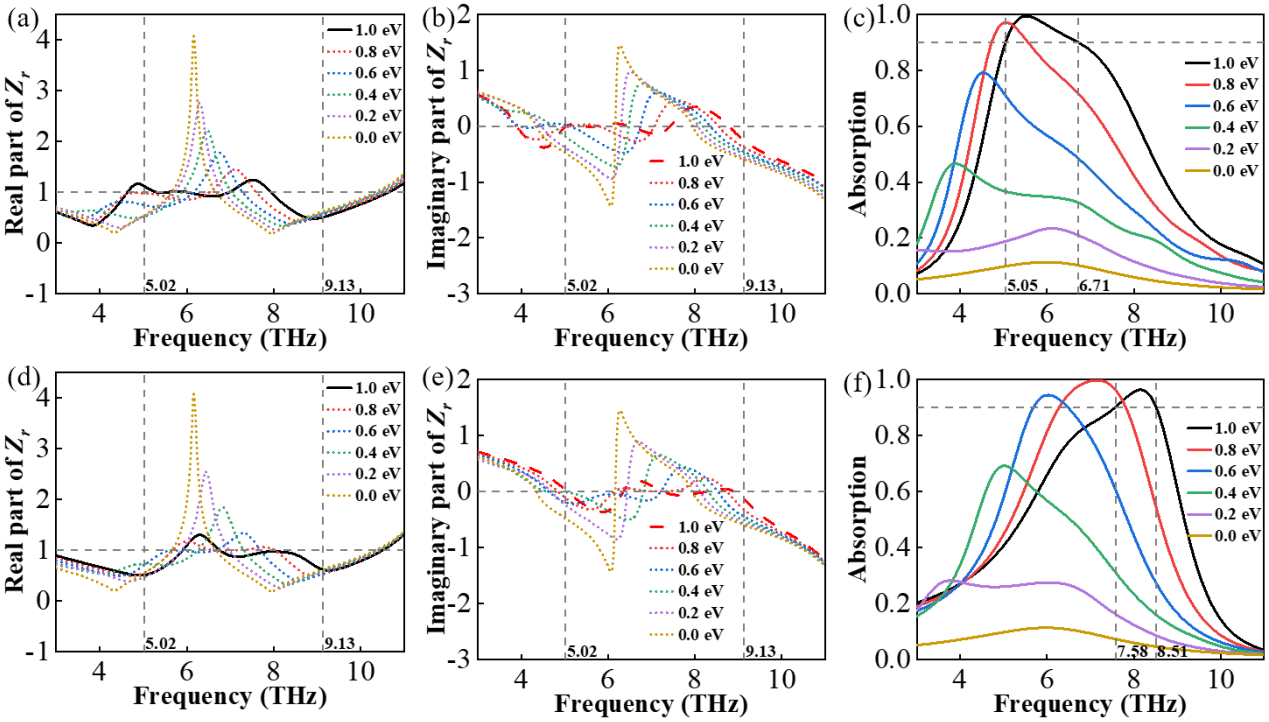

Fig. 5. (a) Real and (b) imaginary parts of the relative impedance and (c) absorption spectrum when E_{F1} is set to be 0 eV while E_{F2} is changed from 0 eV to 1 eV. (d) Real and (e) imaginary parts of the relative impedance and (f) absorption spectrum when E_{F2} is set to be 0 eV while E_{F1} is changed from 0 eV to 1 eV (colour online)

Fig. 6 shows another mode of modulating the absorption frequency. When E_{F1} is set to be 1 eV, and E_{F2} is increased from 0 eV to 1 eV, it can be seen from Fig. 6(a-b) that it is evident that as E_{F2} is increased, the real part of the relative impedance gradually converges to 1 in the low-frequency region while it stabilizes near 1 in

the high-frequency region. Simultaneously, the imaginary part converges to 0 in the low-frequency region but remains unchanged in the high-frequency region. This behavior corresponds well to the absorption performance depicted in Fig. 6(c), transitioning gradually from high-frequency partial absorption to broadband absorption. Conversely, as shown in Fig. 6(d-e), when E_{F2} is set to be 1 eV, and E_{F1} is increased from 0 eV to 1 eV, the changes in the real part and imaginary part of the relative impedance show an opposite trend. The relative impedance gradually converges in the high frequency region. As shown in Fig. 6(f), the absorption of high frequency parts gradually increases, ultimately reaching broadband absorption when $E_{F1} = 1$ eV. These processes show a dynamically continuous tuning capability for independently modulating the intensity of high- and low-frequency absorptance.

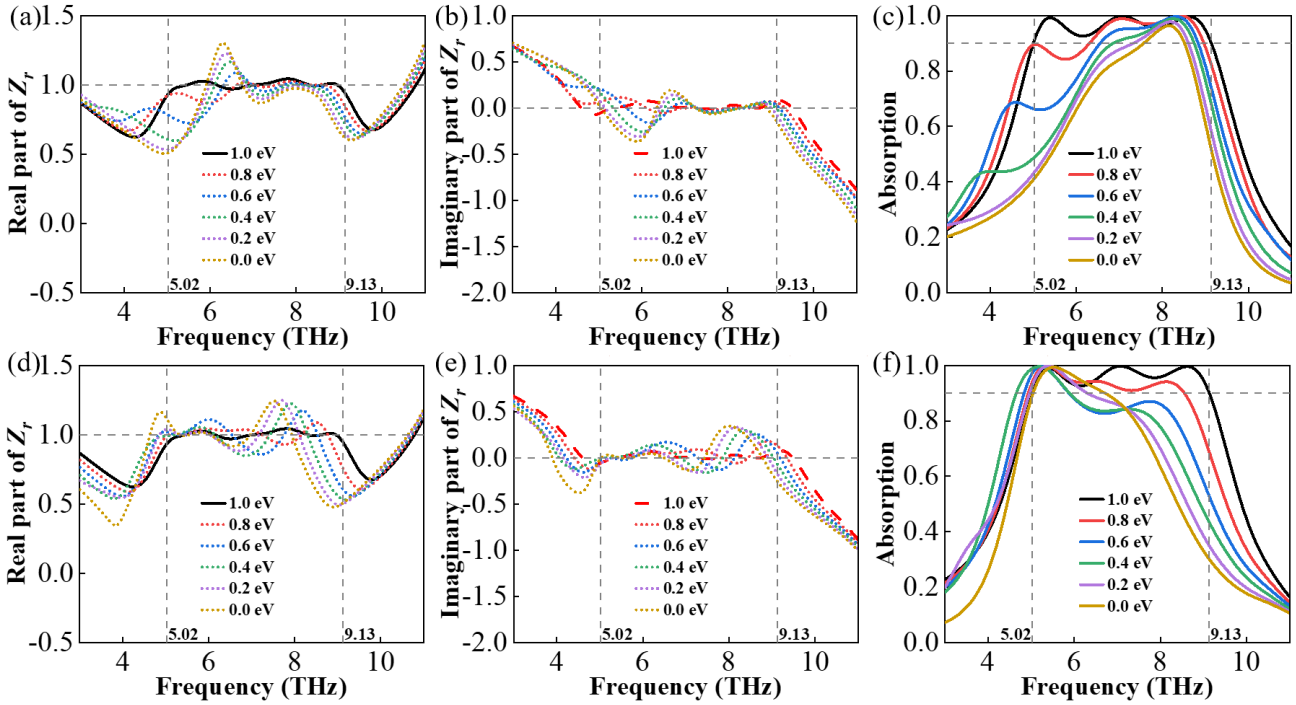

Fig. 6. (a) Real and (b) imaginary parts of the relative impedance and (c) absorption spectrum when E_{F1} is set to be 1 eV while E_{F2} is changed from 0 eV to 1 eV. (d) Real and (e) imaginary parts of the relative impedance and (f) absorption spectrum when E_{F2} is set to be 1 eV while E_{F1} is changed from 0 eV to 1 eV (colour online)

Fig. 7 shows the tunable absorption intensity of the designed absorber. Modulating E_F of the two graphene layers allows for simultaneous adjustments, resulting in stepwise changes in absorption intensity. In Fig. 7(a-b), setting E_{F1} and E_{F2} to 0 eV results in a significant deviation of the real and imaginary parts of the relative impedance from perfect absorption. As indicated by the solid black line in Fig. 7(c), at this point, the absorber achieves a maximum absorption rate of 11%.

Simultaneously setting E_{F1} and E_{F2} to 0.1 eV results in an increased maximum absorption rate of 20%. Similarly, gradually increasing the values of E_{F1} and E_{F2} simultaneously leads to a convergence of the real and imaginary parts of the relative impedance over a broadband range of 5.02-9.13 THz. This results in the absorptance gradually increasing while maintaining broadband absorption. Ultimately, intensity modulation from 11% to 100% is attained.

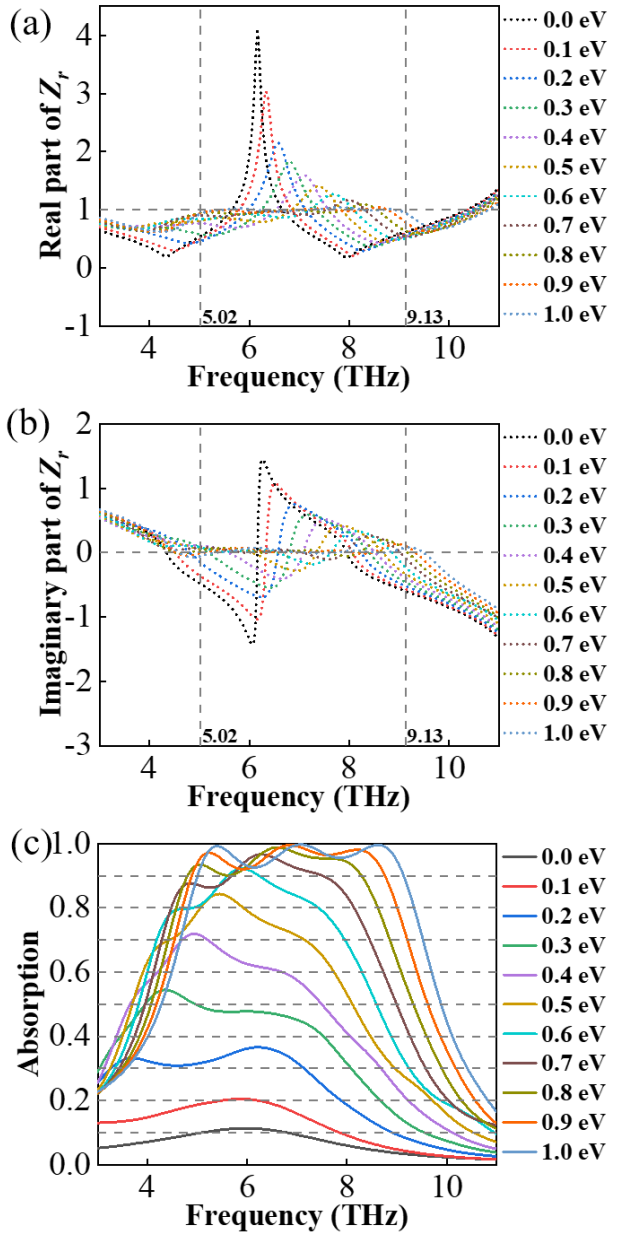

Fig. 7. (a) Real and (b) imaginary parts of the relative impedance and (c) absorption spectrum when E_{F1} and E_{F2} is changed from 0 eV to 1 eV simultaneously (colour online)

Considering the deviation that may occur during the actual manufacturing of the designed absorber, we investigate the impact of thickness of SiO_2 layers on the absorptance. Fig. 8 shows the effect of different thicknesses of SiO_2 layers on the absorptance. As shown in Fig. 8(a-b), even with changes in the thickness of the dielectric layers, the absorber still maintains broadband absorption performance. This shows the characteristic of deviation insensitivity in the designed absorber. This is because the absorption of the metasurface is primarily determined by the properties of graphene, and the influence of the SiO_2 layer on electromagnetic waves is relatively limited. Therefore, small variations in the thickness of SiO_2 do not significantly affect the absorption rates. Meanwhile, as t_1 and t_2 increase, the absorption bandwidth generally experiences a red-shift to varying degrees. This is attributed to structural alterations that disrupt the established phase matching conditions for reflection cancellation which can be formulated as [43]:

$$\varphi_p = \frac{4\pi t_s \sqrt{\varepsilon_r}}{\lambda \cos\theta} \tag{15}$$

where φ_p is the path phase, t_s is the thickness of the SiO_2 layer, ε_r is the relative dielectric constant of the dielectric layer, θ is the incident angle, and λ is the incident wavelength. When the incident wave is a normal plane wave, φ_p, θ, and ε_r remain constant. Therefore, Due to the proportional relationship between t_s and λ, the increase in t_s causes the wavelength of the canceled incident wave to increase, occurring a red shift of the absorption spectrum.

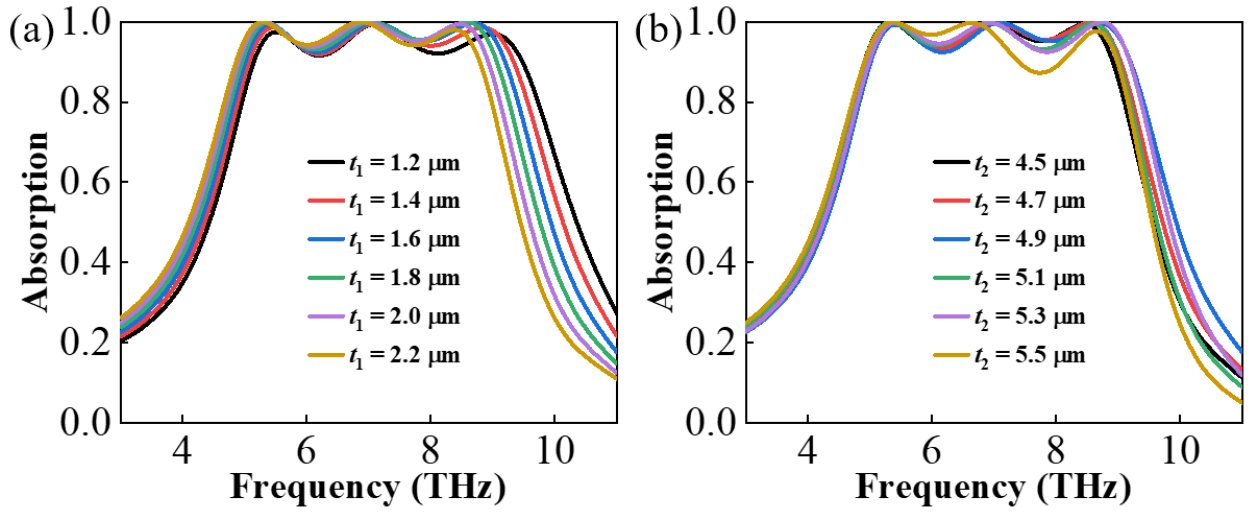

Fig. 8. Absorption spectrum with different (a) thicknesses of SiO_2 layer, t_1 and (b) thicknesses of SiO_2 layer, t_2 (colour online)

Finally, we investigate the impact of incident wave conditions on the absorptance. Fig. 9 shows the absorption spectra at different azimuthal angles and incident angles. As shown in Fig. 9(a), it can be observed that the absorption performance of the designed absorber hardly changes with an increase of the azimuthal angle. This is because the graphene pattern on the metasurface has been carefully designed to be centrosymmetric, resulting in identical responses for both the x-polarized and y-polarized waves. As a result, the absorption performance remains nearly unaffected as the polarization angle changes from 0° to 90°. Fig. 9(b-c) shows the effect of different incident angles on the absorptance in x-polarized and y-polarized modes respectively. With the incident angle continues to increase, the working window experiences a slight narrowing. Even when the incident angle reaches 50°, the absorber is able to maintain a broad absorption band of more than 90% in the range of 5.35-8.71 THz. This demonstrates that the absorber can achieve excellent broadband absorption performance even under a wide range of oblique incident angles.

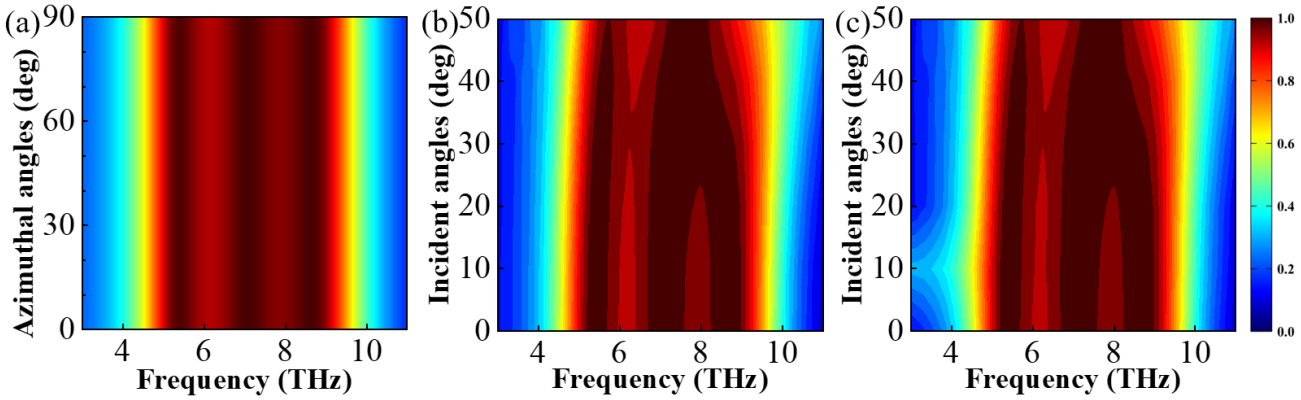

Fig. 9. (a) Absorption spectra at different azimuthal angles. Absorption spectra at different incident angles in (b) x-polarized modes and (c) y-polarized modes (colour online)

Table 1 provides a visual comparison of the absorption performance between the designed absorber and the other absorbers. It can be seen from the table that the previous broadband absorbers do not achieve a working bandwidth surpassing 4 THz. The proposed absorber evidently achieves a wider absorption bandwidth. Concerning frequency modulation capability, most broadband absorbers lack comprehensive investigation. The proposed absorber not only enables a wide frequency modulation range but also provides multiple modulation modes. Concerning intensity modulation, the proposed absorber has a broader frequency modulation range compared to previous absorbers and can maintain broadband absorption while modulating.

Table 1. Comparisons of the designed absorber with other graphene-based absorbers

References	Materials Used	Absorption bandwidth (>90%) (THz)	Frequency modulation range (THz)	Intensity modulation range
[24]	Single graphene layer	0.5	0	40%-90%
[25]	Triple graphene layers	2.66	0	0
[26]	Double graphene layers	1.96	0	52%-100%
[27]	Single graphene layer	3.71	0	0
[28]	Single graphene layers	3.10	1.15	0
[29]	Single graphene layer	3.04	0	15%-100%
This work	Double graphene layers	4.11	4.11	11%-100%

4. Conclusions

In summary, we propose a broadband tunable absorber utilizing double-layer graphene working in the THz band. The absorber exhibits an absorptance of over 90% in the frequency range of 5.02-9.13 THz, providing a remarkable bandwidth of 4.11 THz. By modulating E_F of two graphene layers, independently or concurrently modulating the absorptance at low and high frequencies and absorption intensity modulation from 11% to 100% maintaining broadband absorption can be achieved. Furthermore, the absorber exhibits insensitivity to both azimuthal angle and incident angle, and maintains a broadband absorption performance even when subjected to incident x-polarized and y-polarized waves at large angles.

References

[1] Z. Y. Chen, S. B. Cheng, H. F. Zhang, Z. Yi, B. Tang, J. Chen, J. G. Zhang, C. J. Tang, Physics Letters A **517**, 7 (2024).

[2] N. S. B. Ishak, F. C. Seman, S. K. Yee, N. F. B. Zainal, N. A. B. Awang, N. Zalkepali, Optical Materials **157**, 11 (2024).

[3] W. J. Wang, K. X. Sun, Y. Xue, J. Lin, J. K. Fang, S. N. Shi, S. Zhang, Y. P. Shi, Optics Communications **556**, 16 (2024).

[4] N. Wang, T. Peng, J. Huang, M. Zhang, H. Su, L. Li, H. W. Liang, Optics Communications **559**, 5 (2024).

[5] W. J. Gao, C. Han, X. Y. Lu, Z. Chen, IEEE Open Journal of the Communications Society **5**, 3089 (2024).

[6] J. Seddon, L. Hale, H. Jung, S. Norman, I. Brener, A. Seeds, C. Renaud, O. Mitrofanov, Optics Express **6**(32), 9809 (2024).

[7] Y. X. Chen, Q. K. Wang, K. Y. Wu, ACS Sensors **12**(9), 6572 (2024).

[8] J. B. Pendry, D. Schurig, D. R. Smith, Science **5781**(312), 1780 (2006).

[9] Y. C. Kim, S. W. Jun, S. J. Park, Y. H. Ahn, Optics Express **27**(32), 48915 (2024).

[10] J. Y. Chai, Z. F. Lin, G. G. Kang, Journal of Physics D-Applied Physics **50**(57), 10 (2024).

[11] Z. Pan, J. Zhu, Physica Scripta **1**(99), 11 (2024).

[12] W. K. Xie, Q. Tang, J. L. Xie, Y. Fei, H. J. Wan, T. Zhao, T. P. Ding, X. Xiao, Q. Y. Wen, Nature Communications **1**(15), 8 (2024).

[13] S. Banerjee, P. Dutta, S. Basu, S. K. Mishra, B. Appasani, S. Nanda, Y. I. Abdulkarim, F. F. Muhammadsharif, J. Dong, A. V. Jha, N. Bizon, P. Thounthong, Symmetry-Basel **1**(15), 14 (2023).

[14] J. W. Chen, J. D. Hu, X. H. Deng, J. R. Yuan, T. B. Wang, Journal of Modern Optics **6**(67), 547 (2020).

[15] Y. Mou, X. Y. Yang, M. Vega, R. Zapata, B. Gallas, J. F. Bryche, A. Bouhelier, M. Mivelle, Nano Letters **25**(24), 7564 (2024).

[16] N. I. Landy, S. Sajuyigbe, J. J. Mock, D. R. Smith, W. J. Padilla, Physical Review Letters **20**(100), 4 (2008).

[17] H. Tao, N. I. Landy, C. M. Bingham, X. Zhang, R. D. Averitt, W. J. Padilla, Optics Express **10**(16), 7181 (2008).

[18] Z. Weng, Y. S. Guo, Materials **8**(12), 10 (2019).

[19] J. Y. Jung, J. Lee, D. G. Choi, J. H. Choi, J. H. Jeong, E. S. Lee, D. P. Neikirk, IEEE Photonics Journal **6**(7), 10 (2015).

[20] K. S. Novoselov, A. K. Geim, S. V. Morozov, D. Jiang, Y. Zhang, S. V. Dubonos, I. V. Grigorieva, A. A. Firsov, Science **5696**(306), 666 (2004).

[21] G. M. Cao, X. R. Liu, W. H. Liu, Q. F. Li, X. Li, X. L. Wang, Carbon **124**, 57 (2017).

[22] F. Chen, Y. Z. Cheng, H. Luo, Materials **4**(13), 11

(2020).
[23] E. Watanabe, S. Yamaguchi, J. Nakamura, A. Natori, Physical Review B **8**(80), 6 (2009).
[24] Q. H. Zhou, S. Zha, P. G. Liu, C. X. Liu, L. A. Bian, J. H. Zhang, H. Q. Liu, L. Ding, Materials **12**(11), 8 (2018).
[25] L. Liu, W. W. Liu, Z. Y. Song, Journal of Applied Physics **9**(128), 6 (2020).
[26] J. Xu, Z. J. Qin, M. Chen, Y. Cheng, H. Q. Liu, R. H. Xu, C. X. Teng, S. J. Deng, H. C. Deng, H. Y. Yang, S. L. Qu, L. B. Yuan, Optical Materials Express **10**(11), 3398 (2021).
[27] B. K. Wang, K. Gai, R. X. Wang, F. Yan, L. Li, Optics and Laser Technology **154**, 6 (2022).
[28] H. L. Ren, S. J. Ji, J. Zhao, H. D. Dai, Physica Scripta **7**(98), 11 (2023).
[29] Z. P. Ding, W. Su, H. Wu, W. L. Li, Y. H. Zhou, L. P. Ye, H. B. Yao, Materials Science in Semiconductor Processing **163**, 7 (2023).
[30] S. Sur, R. Bhattacharya, Engineering Research Express **4**(6), 18 (2024).
[31] W. W. Liu, Z. Y. Song, Carbon **174**, 617 (2021).
[32] J. F. Wang, T. T. Lang, T. T. Shen, C. Y. Shen, Z. Hong, C. C. Lu, Applied Sciences-Basel **2**(10), 10 (2020).
[33] M. A. Ordal, R. J. Bell, R. W. Alexander, Jr., L. L. Long, M. R. Querry, Applied Optics **24**(24), 4493 (1985).
[34] L. M. Qi, C. Liu, S. M. A. Shah, Carbon **153**, 179 (2019).
[35] Y. Yang, J. Li, J. N. Li, J. Huang, Y. T. Zhang, L. J. Liang, J. Q. Yao, Optics and Lasers in Engineering **127**, 7 (2020).
[36] S. A. Mikhailov, K. Ziegler, Physical Review Letters **1**(99), 4 (2007).
[37] D. P. Zhang, Z. Li, K. F. Fan, T. Chen, B. W. Jia, S. B. Pan, Y. Tang, AIP Advances **2**(12), 7 (2022).
[38] A. B. Asl, D. Pourkhalil, A. Rostami, H. Mirtaghioglu, Journal of Computational Electronics **2**(20), 864 (2021).
[39] X. H. Deng, J. T. Liu, J. Yuan, T. B. Wang, N. H. Liu, Optics Express **24**(22), 30177 (2014).
[40] Y. Zhang, Y. J. Feng, B. Zhu, J. M. Zhao, T. Jiang, Optics Express **19**(22), 22743 (2014).
[41] S. S. Zhuo, Z. M. Liu, F. Q. Zhou, Y. P. Qin, X. Luo, C. Ji, G. X. Yang, R. H. Yang, Y. D. Xie, Optics Express **26**(30), 47647 (2022).
[42] R. Meservey, P. M. Tedrow, Journal of Applied Physics **5**(40), 2028 (1969).
[43] L. Huang, D. R. Chowdhury, S. Ramani, M. T. Reiten, S. N. Luo, A. J. Taylor, H. T. Chen, Optics Letters **2**(37), 154 (2012).

*Corresponding author: gaoyachen@hlju.edu.cn